Validity of Machine Learning in the Quantitative Analysis of Complex Scanning Near-Field Optical Microscopy Signals Using Simulated Data

Xinzhong Chen,[1,*] Richard Ren,[1] and Mengkun Liu[1,2,†]

[1] *Department of Physics and Astronomy, Stony Brook University, Stony Brook, New York 11794, USA*
[2] *National Synchrotron Light Source II, Brookhaven National Laboratory, Upton, New York 11973, USA*

(Received 10 September 2020; accepted 8 December 2020; published 4 January 2021)

Scattering-type scanning near-field optical microscope (s-SNOM) is a modern technique for subdiffractional optical imaging and spectroscopy. Over the past two decades, tremendous efforts have been devoted to modeling complex tip-sample interactions in s-SNOM, aimed at understanding the electrodynamics of materials at the nanoscale. However, due to complexities in analytical methods and the limited computation power for fully numerical simulations, compromises must be made to facilitate the modeling of tip-sample interaction, such as using quasistatic approximation or unrealistic tip geometries. In this paper, we apply a variety of widely utilized machine-learning methods, including k nearest neighbor and feed-forward neural network etc. to study the phase-resolved spectroscopic near-field response. With only a small set of training data, which is simulated using the finite-dipole model, we demonstrate that the relation between the experimental near-field signal and sample optical constant can be one to one mapped without the need for tip modeling: for a given material with a moderate dielectric function, its complex near-field spectrum can be accurately determined within the mid-IR spectral range, and vice versa. Our preliminary study sets the stage for future exploration using real experimental data. Our method is beneficial for processing the increasing amount of data accumulated across many research groups and especially useful for user facilities such as synchrotron-based national laboratories where a large amount of data is generated on a daily basis.

DOI: 10.1103/PhysRevApplied.15.014001

I. INTRODUCTION

Scattering-type scanning near-field optical microscopy (s-SNOM) has gained significant popularity among different research disciplines in the last two decades [1–3]. It is a powerful technique that offers optical resolution far beyond the diffraction limit, which is achieved by coupling light to a sharp atomic force microscope (AFM) tip with an apex radius as small as a few nanometers [4]. Unlike its far-field technique counterparts where the light directly interacts with the sample specimen, in s-SNOM the complex near-field tip-sample interaction plays the dominant role. The AFM tip functions as an antenna that localizes the incident light tightly under its apex through the lighting-rod effect. The near-field tip-sample interaction modifies the radiation of the tip, which can be detected from the scattering signal in the far field. Through the study of this tip-modulated radiation, the local dielectric properties can then be deduced [5–8]. Besides monochromatic imaging [9–15], the broadband spectroscopic capability of s-SNOM has led to a rich body of research activities especially in the technologically relevant near-IR to terahertz (THz) regime [16–20]. A typical experimental setup is demonstrated in Fig. 1(a), where the broadband light source is coupled to an asymmetric Michelson interferometer and an AFM. The detector collects the interference signal between the tip-scattered light and the reference light reflected off a scanning mirror. The Fourier transform of such an interferogram demodulated at the higher harmonics ($n>1$) of the tip-tapping frequency yields the frequency-domain near-field spectrum.

Analytical models attempting to quantitatively describe the near-field tip-sample interaction have been proposed and improved over the years [21–25]. In the most simplified model, the entire tip is reduced to a sphere located at its apex [21]. In the quasistatic limit, the scattered field can be analytically calculated. It was soon realized that the sphere did not accurately capture the elongated shape of the tip shank, and therefore, led to inaccurate results. Consequently, more sophisticated models such as the finite-dipole model were proposed where the tip is approximated as a spheroid [22]. To date, several physically rigorous models are developed and better quantitative descriptions have been achieved [23–25]. However, there are still many constraints in these methods. For example,

*xinzhong.chen@stonybrook.edu
†mengkun.liu@stonybrook.edu

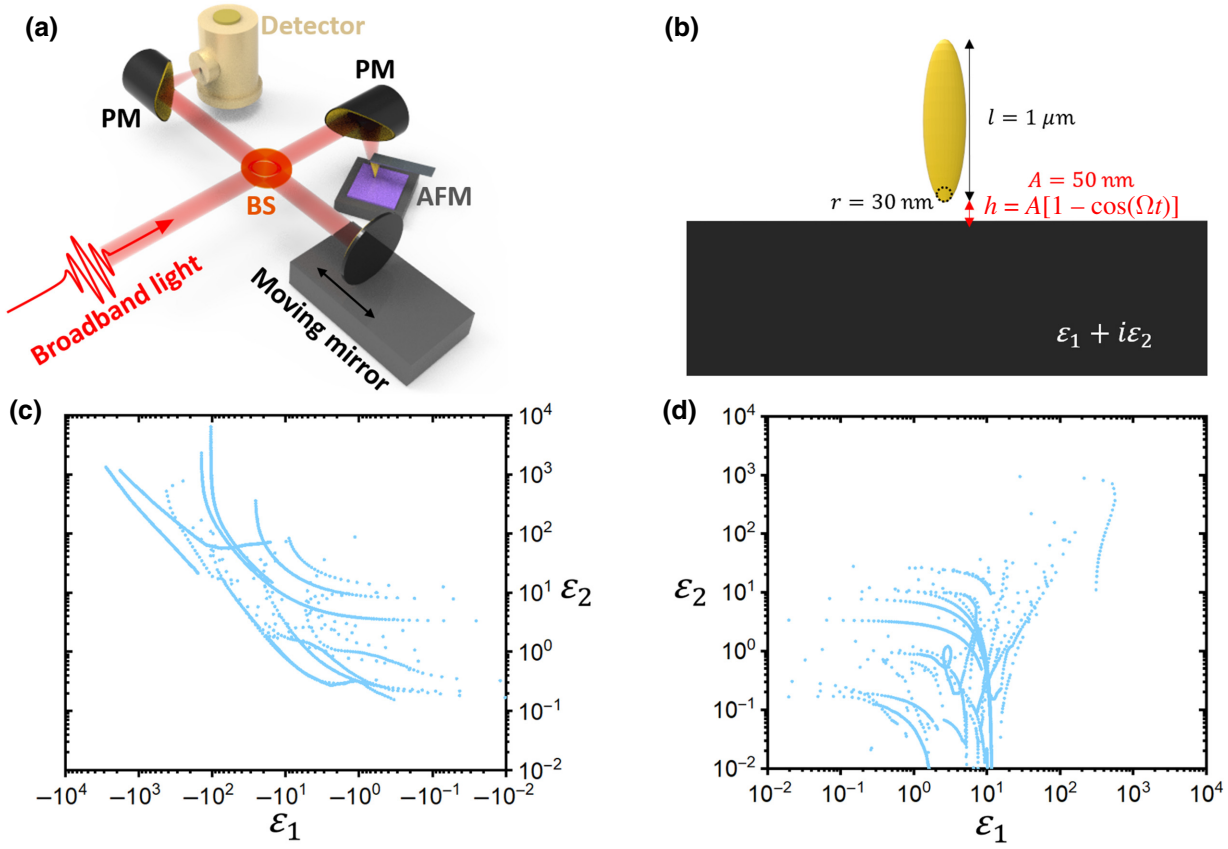

FIG. 1. (a) Schematics of a typical broadband s-SNOM setup. BS, beam splitter; PM, parabolic mirror. (b) Schematics of the finite-dipole model where the tip is approximated as an elongated spheroid of 1 μm length and 30 nm apex radius. The tip oscillates at its mechanical resonance frequency Ω with a 50 nm amplitude. (c), (d) Population distribution of all the training data in the ε space.

the quasistatic approximation is usually adopted, and thus the retardation effect is ignored to simplify the problem. In reality, the length of the real AFM probe (tip shank) is in the order of 10 μm, often longer or comparable to the incident wavelength in the IR frequency. Consequently, the assumption that the incident wavelength is much longer than the tip size is not always appropriate. The cantilever, realistic cone angle, and multiple reflections between the tip and sample are also hard to include in analytical models. Furthermore, materials commonly exhibit anisotropy, which is still not carefully handled in the existing models. Although these shortcomings can be circumvented by using the full-wave numerical Maxwell-equation solvers [26–30], the requirement for time and computation power is often deemed impractical for many researchers.

Machine learning (ML) is a form of artificial intelligence that utilizes computer algorithms based on statistics to extract hidden information from data. It has been one of the fastest developing technologies in recent decades owing to the rapidly advancing computer hardware. ML has also found itself widely applicable in most scientific disciplines, including physics [31–33]. More specifically, it has been demonstrated that ML can be employed in nanophotonics research. For example, feed-forward neural networks (FFNNs) have been utilized to predict the response of metamaterials or nanostructures and inversely engineer the desirable spectral features [34–37]. Compared to conventional approaches, such as trial experiments or numerical simulations using full-wave solvers, ML often yields satisfactory accuracy and orders of magnitude higher time efficiency. In this paper, we aim to demonstrate that ML can be applied to accurately describe near-field tip-sample interactions and its spectroscopic response. A variety of the most well-known ML algorithms including k nearest neighbor (kNN), random forest, decision tree, polynomial regression, and FFNN are tested. Even though most of them yield reasonably accurate predictions, we find FFNN to be the superior method. Through a limited amount of training data only, we show that the relationship between the s-SNOM contrast and the sample optical constant can be fully mapped. The fine detail of the AFM tip is not a necessity of the training process, which significantly reduces the complexity of the problem. Given the fact that currently there are many s-SNOM users and facilities around the globe, we envision that the ML techniques

can be helpful to progress the current research trend and yield faster data-experiment turnaround time.

II. DATA ACQUISITION

In this pilot study, instead of using real experimental data, we demonstrate the viability of the proposed ML techniques using pseudodata generated from the finite-dipole model [22]. The reason is twofold: firstly, with the analytical model, the generation of the training data set is exact and fast. Therefore, the ML prediction can be easily verified by comparing it to the analytical calculations for quantitative accuracy check. This is critical for evaluating the efficacy of the ML procedures; secondly, the finite-dipole model has been shown in multiple studies to have reasonably good agreement with experimental data [38–41]. Thus, it is a good representation of the tip-sample interaction and can serve as comparative guidance for future ML studies using real experimental data.

As schematically depicted in Fig. 1(b), in the finite-dipole model the tip is approximated by a metallic elongated spheroid. The tip-scattered field is captured by the effective tip polarizability

$$E_{\text{scatt}} = \alpha_{\text{eff}} E_{\text{inc}} \propto \frac{1}{2}\frac{\beta f_0}{1-\beta f_1} + 1, \tag{1}$$

where $\beta = (\varepsilon - 1)/(\varepsilon + 1)$ is the sample response function and $\varepsilon = \varepsilon_1 + i\varepsilon_2$ is the sample dielectric function. f_0 and f_1 are geometric factors that depend on tip length, apex radius, and tip-sample distance [22,42]. Assuming a harmonic motion of the tip, the scattered field E_{scatt} as a function of time demodulated at nth harmonics of tip oscillation frequency Ω

$$S_n = \int_0^{2\pi/\Omega} E_{\text{scatt}}(t) e^{-in\Omega t} dt \tag{2}$$

can be directly compared to the experimental data. For the calculations throughout the paper, we use the following fixed parameters: tip apex radius $r = 30$ nm, tip length $l = 1\ \mu$m, and tip oscillation amplitude $A = 50$ nm. These are common choices of parameters in the literature that yield comparable results to data acquired with commercial AFM tips (e.g., NanoWorld Arrow$^{\text{TM}}$ NCPt).

Besides the analytical models, another necessary ingredient for generating pseudodata is the dielectric functions of sample materials, which are readily accessible from the *Handbook of Optical Constants of Solids* [43]. Without loss of generality, we select 12 common isotropic materials as our samples. They include noble metals (gold and platinum), semiconductors (Si, ZnSe, GaAs, and InAs), and insulators (SiO_2, CuO_2, MgO, $SrTiO_3$, CaF_2, and KBr). Gold is used as the reference material to normalize the near-field spectra of other samples. For Si, we include intrinsic Si and phosphorus-doped Si with carrier density 10^{17} cm^{-3}, 10^{18} cm^{-3}, 10^{19} cm^{-3}, 10^{20} cm^{-3}, and 10^{21} cm^{-3}. The dielectric function of doped Si is described by the Drude model with a carrier density-dependent mobility, as demonstrated in previous studies [44–46].

The spectra are calculated with approximately 3 cm^{-1} resolution, which is experimentally practical. The population distribution of the training data can be visualized by the scattered plot of the ε space as shown in Figs. 1(c) and 1(d). In total, there are 13 849 data points. The distribution is generally sparse. The regime that we put the most attention to is near the origin where both the real and imaginary parts of ε are relatively small (e.g., $|\varepsilon| < 10^2$) since the near-field response shows significant variation in this regime. It is well known that for highly metallic or dielectric materials (e.g., $|\varepsilon| > 10^2$), the s-SNOM contrast asymptotically approaches unity. This is evident by examining the finite-dipole model as β approaches unity for large $|\varepsilon|$ values. The dielectric functions and the corresponding near-field spectra calculated using the finite-dipole model for different materials are displayed in Fig. 2.

One could immediately raise the concern that the pseudodata we generate from the finite-dipole model is noiseless, which is not a good representation of real experimental data. To verify that ML algorithms can work well with noisy data, we artificially add random noise to the pseudodata to imitate realistic data (see Appendix A). In the following sections, the dielectric functions and the near-field spectra are used as the training data for our regression ML algorithms. The goal is to accurately predict one from the other without evoking the analytical model. The result calculated directly from the analytical model is used as a quantitative gauge for how accurate our trained ML models are.

III. RESULTS AND DISCUSSIONS

A. *k* nearest neighbor

First we train with the pseudodata using a computationally inexpensive ML algorithm—*k*NN. *k*NN is a popular and robust nonparametric ML algorithm that is easy to implement for both classification and regression problems [47,48]. In this algorithm, the predicted output value for a given input depends on the *k* nearest neighbors in the training data. Here we use distance-weighted *k*NN for $k = 15$ on our training data. For our given training data, we find that different searching algorithms such as Ball Tree, KD Tree, and brute-force searching yield similar results and time efficiency because the size of the data set is relatively small.

Using the noiseless data from Fig. 2, prediction of S_n–ε relation in the most relevant ε range ($-100 < \varepsilon_1 < 100$, $0 < \varepsilon_2 < 100$) is made and shown in Figs. 3(a) (real) and 3(b) (imaginary) in double-log scale. The same *k*NN

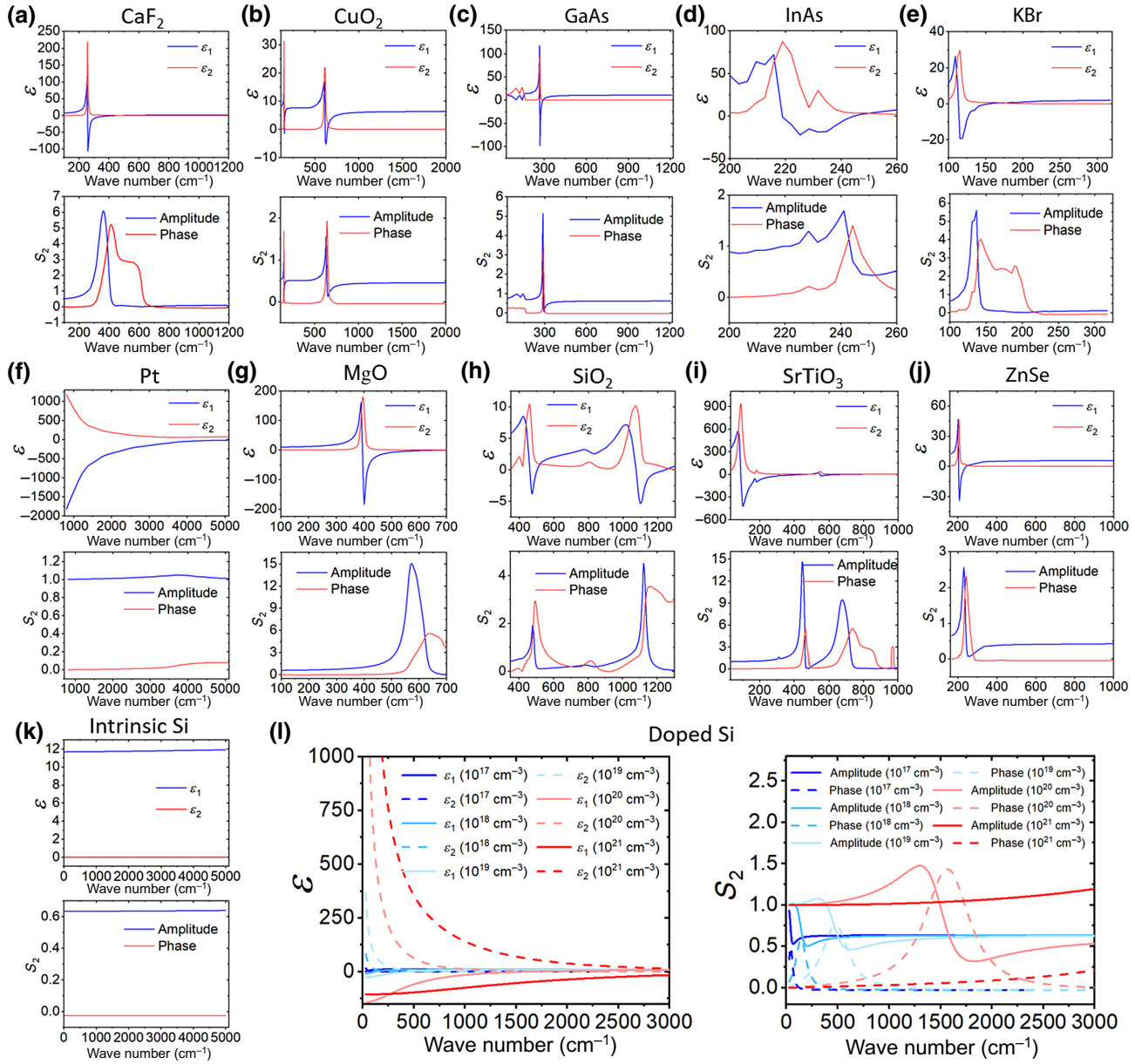

FIG. 2. IR and THz dielectric functions of sample materials obtained from Ref. [43] and the corresponding near-field spectra calculated by the finite-dipole model. Gold is used as the reference for normalizing the spectra.

algorithm is implemented on the noisy data and results (not shown) are practically identical because the averaging over 15 samples effectively suppresses the noise. Analytically calculated real and imaginary parts of S_n using Eqs. (1) and (2) are shown in Figs. 3(c) and 3(d), respectively, as a comparison. The absolute difference, Δ, between the kNN prediction and the analytical solution is plotted in Figs. 3(e) and 3(f). It is evident that kNN can efficiently grasp the overall feature of $S_n(\varepsilon)$. However, some fine details can be overlooked due to the insufficient amount of data and specific data distribution. For example, a strong resonance near $\varepsilon_1 = -1$ and $\varepsilon_2 = 0$ can be seen in the analytical solution but is weakened in the kNN predicted result. In addition, the predicted result seems to suffer from discontinuity in certain regions. This is a common artifact in kNN due to the specific training data distribution. This artifact can be avoided when a larger and more evenly distributed training data set is available. However, extra cautions must be exercised when choosing the appropriate searching algorithm in kNN on large training data set as the searching can be time consuming for a large training dataset.

Similar to kNN, popular ML algorithms like random forest, decision tree, support vector machine, andpolynomial regression can, in principle, be applied to perform regression tasks. We also explore these options (see

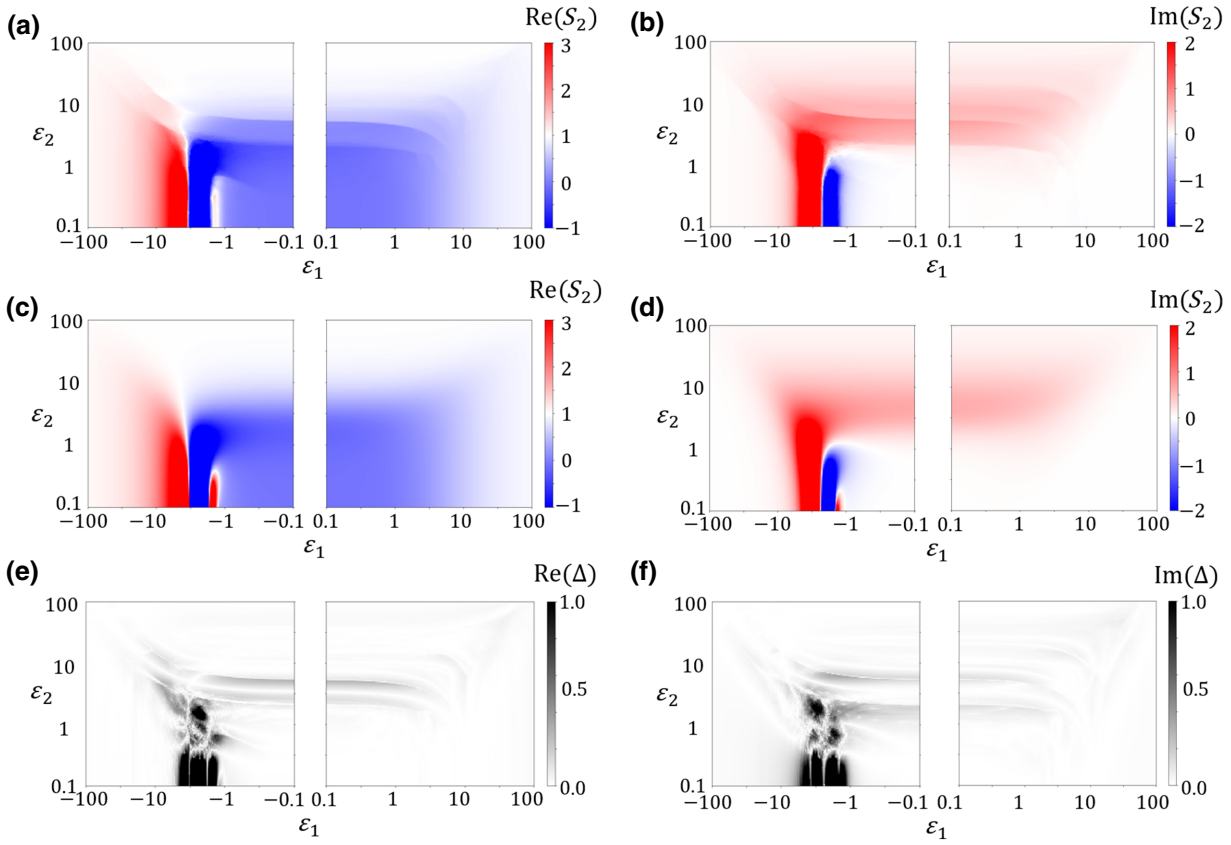

FIG. 3. (a), (b) Predicted real part and imaginary part of S_2 using kNN with $k = 15$. S_2 is encoded as the color map, whereas ε_1 and ε_2 are the x and y axis, respectively. (c), (d) Analytically calculated real and imaginary part of S_2, respectively. (e), (f) Difference between the prediction by ML and the analytical solution.

Appendix B) with our training data and conclude that, given the current training data, the predictability of these algorithms is not superior compared to kNN.

B. Fully connected feed-forward neural network

At present, one ML method that truly stands out is multilayer FFNN, which is also often referred to as multilayer perceptrons. This method has been demonstrated to excel in numerous situations from the medical industry to finance and sciences due to its ability to fit complex functions [49–51]. Next we demonstrate that FFNN is the superior algorithm for our purpose.

The optimal FFNN architecture depends highly on the specific problem and dataset. As a proof of concept, we train our data using a FFNN with five hidden layers and 20 neurons per layer as schematically shown in Fig. 4(a). The hyperbolic tangent sigmoid function is selected as the activation function and the sum of squared residuals (SSR) is used as the loss function. We find this FFNN to be computationally inexpensive yet sufficiently complex to fit our data. The training data are first normalized to 0 to 1 interval by linear transformation for faster convergence and better accuracy. After the training, the prediction is scaled back by the reverse linear transformation. The Broyden-Fletcher-Goldfarb-Shanno (BFGS) algorithm is implemented to iteratively optimize the FFNN parameters [52]. We find that BFGS exhibits superior performance compared to more common algorithms, such as gradient-descent methods when working with a relatively small dataset such as ours. For larger training datasets, however, BFGS might not be optimal and efficient thus more commonly used techniques such as various algorithms based on gradient descent should be considered. As shown in Fig. 4(b), in a typical learning process, after 2500 epochs, SSR is reduced to 10^{-6} level. After the training, we use the trained FFNN to predict the complex S_2 for ε in the relevant frequency range. The result is shown in Figs. 4(c) and 4(d). Compared to the analytically calculated result [using Eqs. (1) and (2)] in Figs. 3(c) and 3(d), it is evident that FFNN works exceedingly well. Δ for the prediction is plotted in Figs. 4(e) and 4(f). We find that $\Delta \approx 0$ except in a small region where ultrastrong resonance occurs ($-1 < \varepsilon_1 < -5$ and $\varepsilon_2 < 0.5$).

The same training procedure is carried out for the noisy data set and the results are shown in Figs. 5(a) and 5(b)

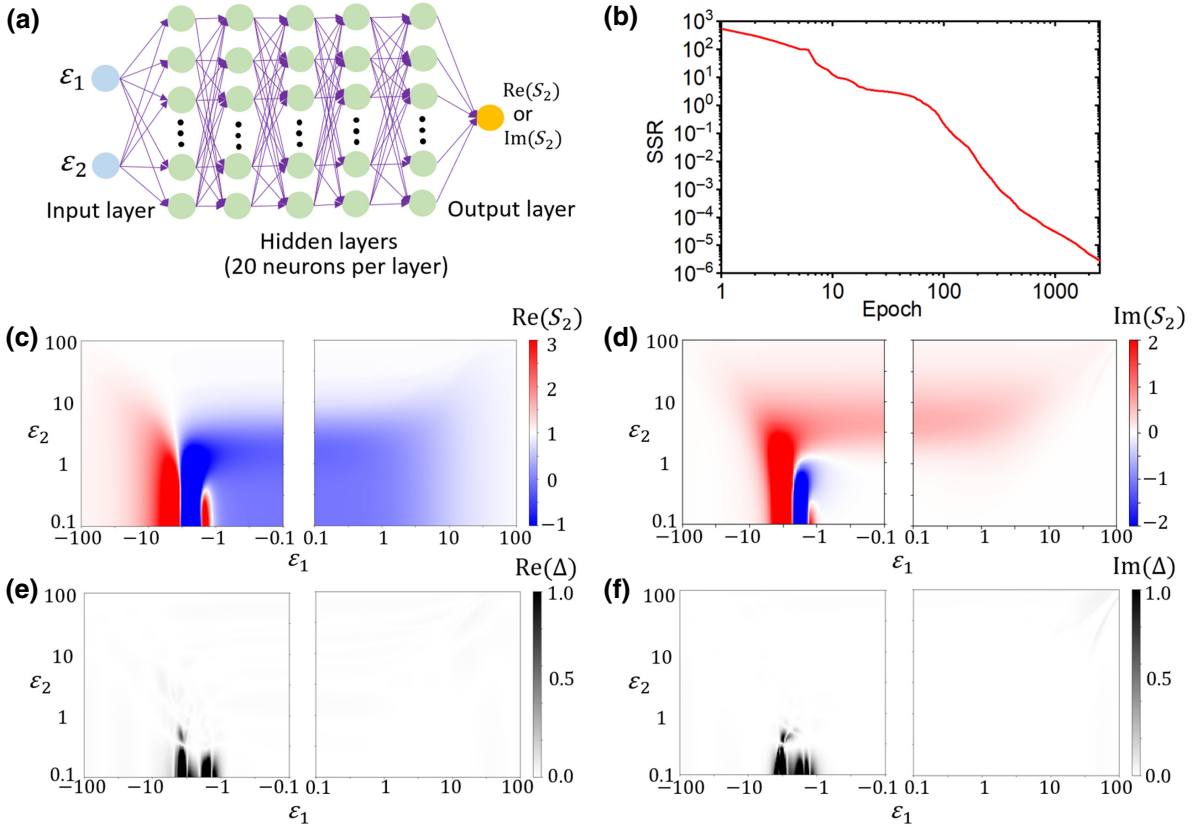

FIG. 4. (a) Schematics of the FFNN architecture. (b) A typical SSR as a function of epoch. (c), (d) Predicted real part and imaginary part of S_2 using FFNN trained with noiseless data, respectively. (e), (f) Absolute difference between the prediction and the analytical solution.

with Δ shown in Figs. 5(c) and 5(d). Compared to training results using noiseless data, Δ shows only a slight increase in the noise level. Note that when working with noisy data, extra care must be taken to avoid overfitting. Given the current noise level, overfitting is not a serious concern. Although we incorporate a practically achievable noise level in the training data, the real experimental data can potentially contain a higher noise level due to

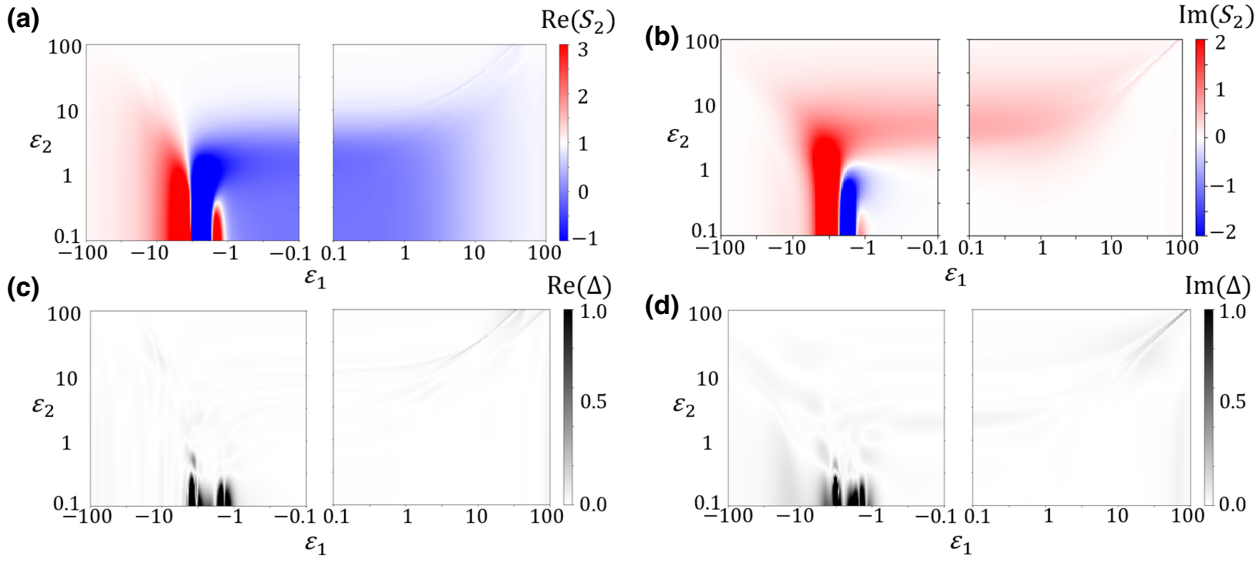

FIG. 5. (a), (b) Predicted real part and imaginary part of S_2 using FFNN trained with noisy data, respectively. (e), (f) Absolute difference between the prediction and the analytical solution.

imperfect optical alignment, light source instability, and so on. In that case, active measures such as regularization or dropout should be implemented to avoid potential overfitting issues.

C. The inverse problem ($S_2 \rightarrow \varepsilon$)

The inverse problem—calculating dielectric function using experimentally measured near-field spectra—is nontrivial. Previous attempts demonstrate reasonable results in a number of cases [5–8,23,53,54]. However, several fundamental issues remain unsolved. For example, there is an inherent inaccuracy in model-based inversion. More importantly, the near-field measurables are single-valued functions of the sample dielectric function, but the reserve is not always valid. Therefore, when attempting to extract dielectric function from measurement, we often face a multivalued problem. This can be easily seen from the analytical calculation results in Figs. 3(c) and 3(d). When $|\varepsilon_1|$ or $|\varepsilon_2|$ approaches approximately 100, $\mathrm{Re}(S_2) \rightarrow 1$ and $\mathrm{Im}(S_2) \rightarrow 0$. That is, as stated previously, when the material is highly metallic or dielectric, the near-field response "saturates" to 1. Under this circumstance, the inversion is fundamentally ill defined.

Fortunately, we are typically not interested in retrieving the dielectric function of noble metals or high dielectric materials as they do not have any other spectral signature at infrared frequencies. Instead, we are interested in materials that exhibit mild or strong resonances. Therefore, we can focus our attention on $S_2 \neq 1$ by imposing a filter on the training data where points with $0.9 < \mathrm{Re}(S_2) < 1.1$ and $-0.1 < \mathrm{Im}(S_2) < 0.1$ and the corresponding ε are omitted from the data set (note that the near-field signal S_2 can be much larger or smaller than 1). We then train the FFNN with the truncated data set. We perform the FFNN training on both the noiseless data set and the noisy data set. The same network architecture shown in Fig. 5(a) is used in the inversion problem. $\mathrm{Re}(S_2)$ and $\mathrm{Im}(S_2)$ are used as inputs and ε_1 or ε_2 the output. After the training is finished, we first use the network to predict the dielectric functions of

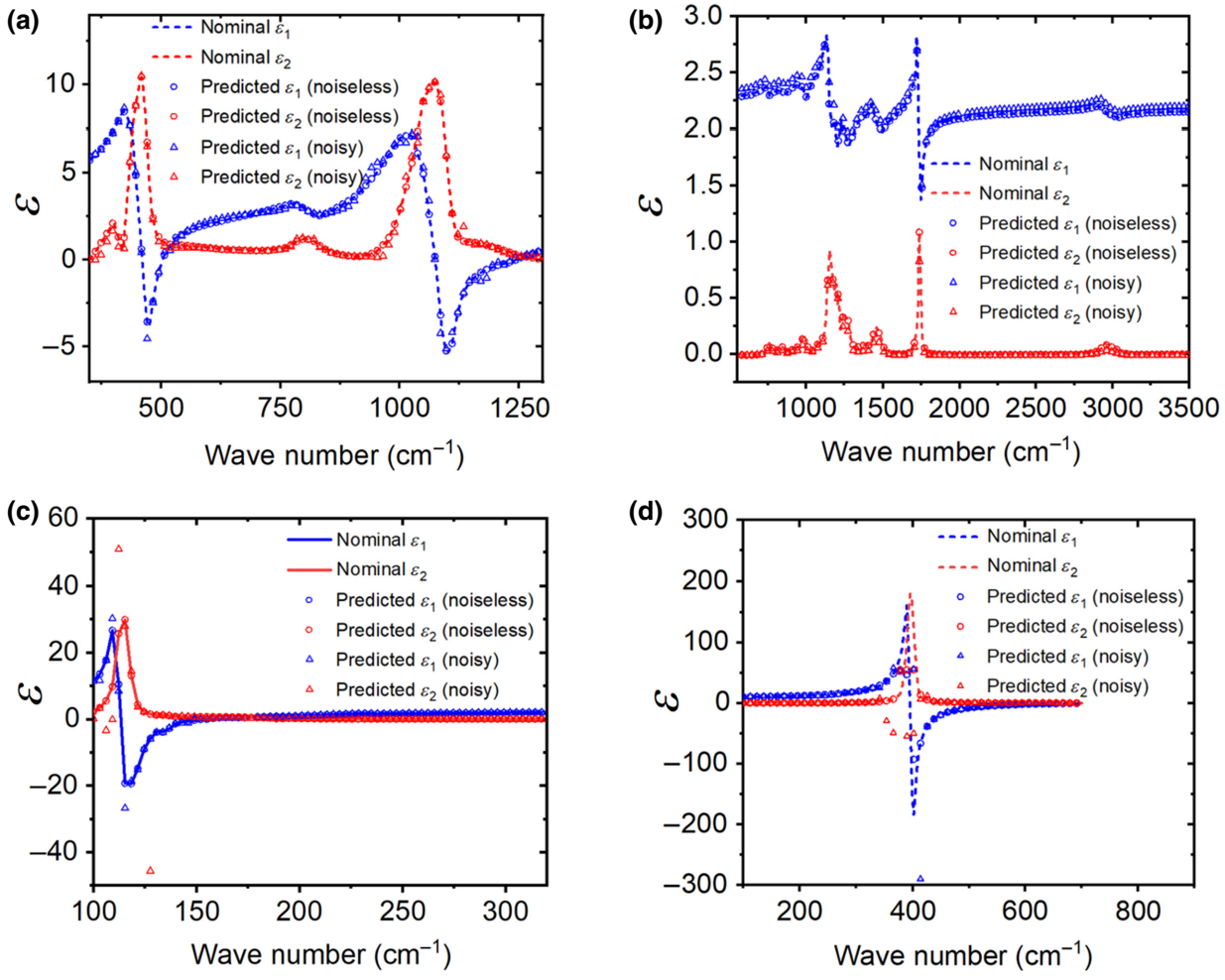

FIG. 6. Nominal dielectric function, predicted dielectric function using noiseless training data, and predicted dielectric function using noisy training data for (a) SiO_2, (b) PMMA, (c) KBr, and (d) MgO.

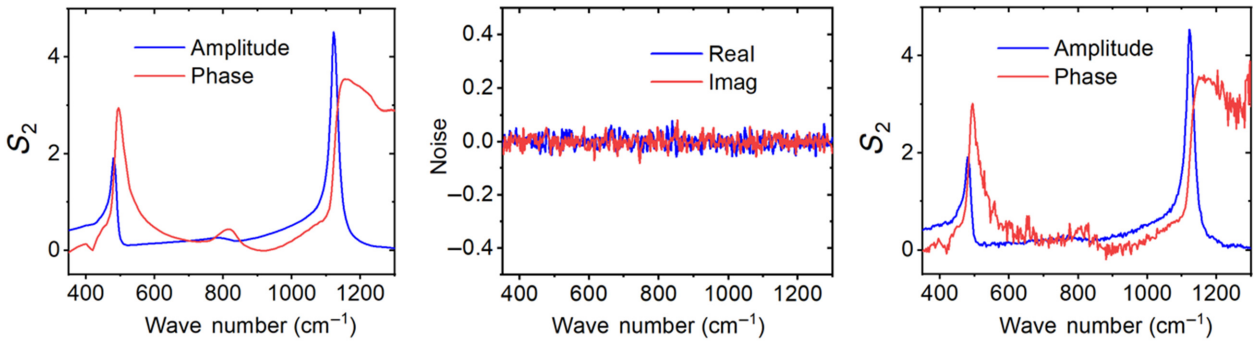

FIG. 7. (a) Noiseless amplitude and phase spectra of SiO_2 in the pseudodataset. (b) Artificially generated random noise centered at 0 with a standard deviation of 0.025. (c) Amplitude and phase spectra of SiO_2 with added random noise to mimic real data.

SiO_2. The nominal value and the predicted values using noiseless and noisy data are shown in Fig. 6(a). For materials with moderate resonance, the prediction accuracy is excellent even with noisy data. The error, which is defined as (predicted value - nominal value)/nominal value, is smaller than 5%. Next, we test a material that is not in the training samples to verify the generality of the trained network. For this purpose, we obtain the infrared dielectric function of PMMA, which exhibits mild resonances in the 600 to 5000 cm^{-1} range, from the literature [55]. Then S_2 for PMMA is calculated using the finite-dipole model and used as input for the trained FFNN. The predicted results of the PMMA dielectric function are shown in Fig. 6(b). The accuracy is similar to the SiO_2 case as expected. For materials with larger $|\varepsilon|$ (e.g., stronger phonon resonances) the inversion gives inaccurate results since we set the training data $S_2 \neq 1$ to avoid the multivalue issue. Indeed, the prediction of ε in KBr and MgO starts to deviate from the nominal values at certain spectral regimes as shown in Figs. 6(c) and 6(d). This problem could potentially be circumvented by imposing additional regulations such as continuity of the dielectric function or Lorentz lineshapes, which remains to be carefully tested. The same attention to potential overfitting should be exercised here, similar to the forward problem in the previous section. In addition, we also explore the inverse problem using other algorithms such as *k*NN (see Appendix C), but even for materials with small or moderate ε values, the accuracy of the inversion is poorer compared to FFNN. FFNN currently remains the most accurate algorithm for both the forward and inverse problem.

IV. CONCLUSION AND OUTLOOK

In our proof-of-principle demonstration here, many effects are yet to be considered. These effects can be studied in the future with real experimental data. For example, how biaxial or uniaxial anisotropy in the dielectric function the near-field response is still understudied [56]. This can be investigated by using the full dielectric tensor as input and experimental data as output for the ML algorithms.

For simplicity, parameters like the tip geometry and oscillation amplitude are fixed in our pseudodata generation procedure. In practice, these parameters are not needed as long as the training data are measured with the same or similar set of commercial AFM tips and oscillation amplitude. If the training data are obtained from different facilities under different conditions, these parameters can be used as inputs for the training as well to account for the relevant effects. Additionally, the ML algorithms can further shed light on problems like optimizing the tip design for enhanced near-field contrast, similar to the optimization procedure in the case of metamaterial design [34–36].

Due to the quasistatic nature of the finite-dipole model, incident wavelength does not explicitly affect the near-field response. One reason why this approximation works well is that only the tip apex plays the dominant role in the near-field tip-sample interaction. However, the usefulness of tip shank cannot be ignored when performing quantitative analysis on the near-field signal. In the near- or mid-IR frequency regime, the wavelength is comparable or even shorter than the tip length, which challenges the validity of quasistatic approximation. The analytical electrodynamic model for realistic tip geometry has shown that retardation is indeed a prominent effect especially for longer tips [23]. The wavelength-dependent near-field response can be studied in ML by using the wavelength as an explicit input. This might be especially relevant for THz s-SNOM [57–59].

Besides spectroscopy, many ML concepts can be implemented in s-SNOM imaging experiments as well. For example, computer vision can be applied to analyzing monochromatic s-SNOM images where a variety of spatial patterns emerge [9,11,12,60,61]. One popular application of s-SNOM is surface-polariton interferometry [10,14,15,62–65], where surface-polariton propagation manifests as interference fringes in the s-SNOM images. Polariton characteristics and consequently materials properties can be deduced from the fringes. This routine analysis is currently performed manually. Computer vision can learn from past images and be applied to automatically identify fringe

patterns in future images at a much more efficient and accurate level where quantities like the polariton wavelength, decay length, and dispersion can be obtained.

In summary, we demonstrate through a limited amount of pseudodata generated from the finite-dipole model that simple ML regression algorithms such as FFNN can be successfully applied to gain good predictability in the near-field analysis. Given a larger training data set with a variety of materials, the outcome is expected to be significantly improved even further. This is experimentally practical because in research labs and user facilities a large amount of data is constantly generated from a variety of samples. More sophisticated ML algorithms can be implemented when the dimension of the problem is increased to include various nontrivial effects. For example, the lateral size and thicknesses of the sample, length scale of the electronic, and phononic inhomogeneity can also be considered in the future learning process once a sufficient amount of experimental data are available.

ACKNOWLEDGMENTS

We acknowledge support from the National Science Foundation under Grant No. DMR-1904576. This work is partly supported by the RISE2 node of NASA's Solar System Exploration Research Virtual Institute under NASA Cooperative Agreement 80NSSC19MO2015. We

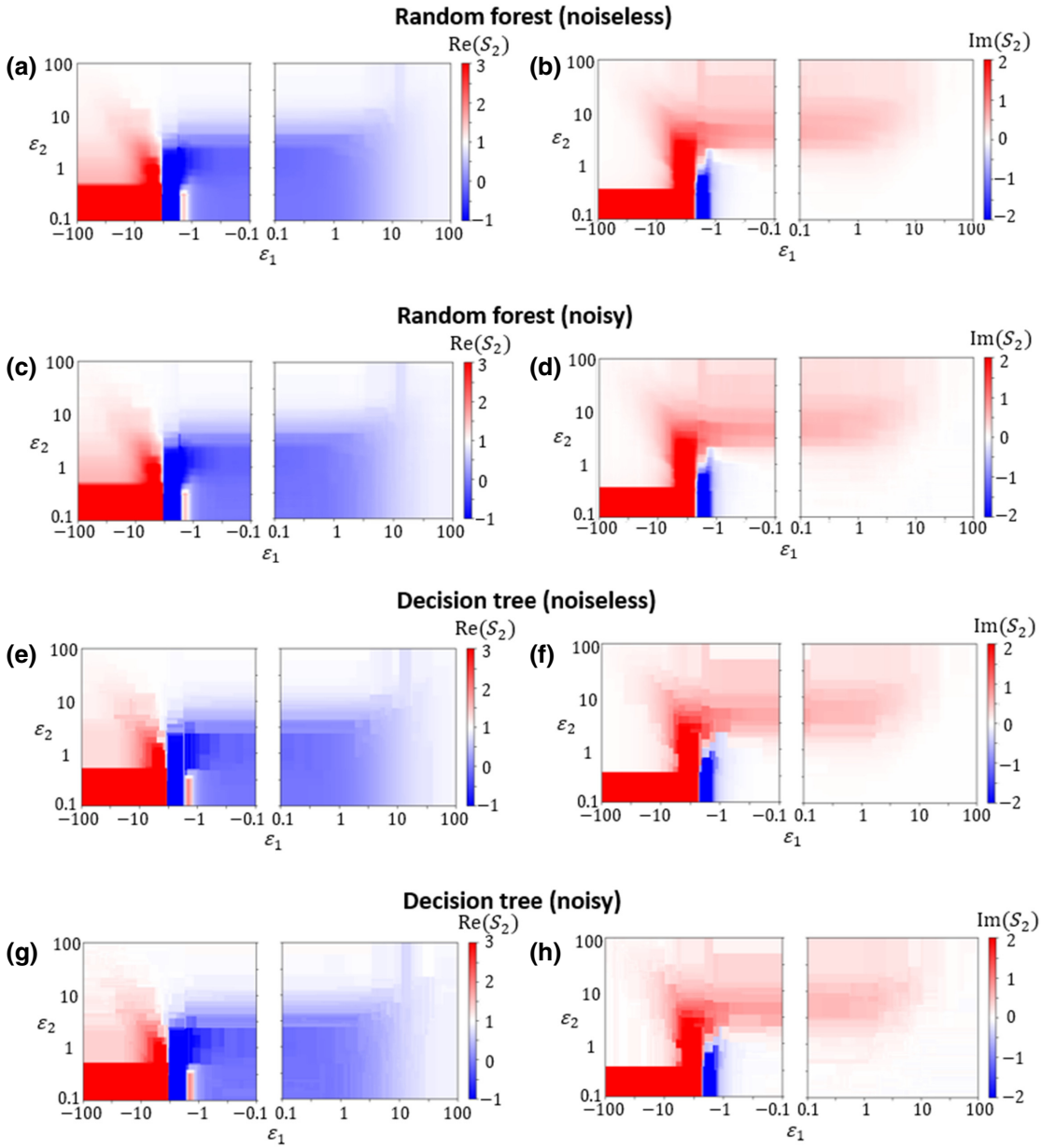

FIG. 8. Predicted real part and imaginary part of S_2 using random-forest regression and decision-tree regression.

also acknowledge the SBU/BNL SEED and OVPR Seed Grant from Stony Brook University.

APPENDIX A: INCLUSION OF RANDOM NOISE

Random noise is generated with a Gaussian distribution centered at 0. The standard deviation is set to 0.025, which is comparable to the real experimental noise level in a well-aligned broadband s-SNOM system [17,19]. The typical data before the noise added is shown in Fig. 7(a). Typical random noise is shown in Fig. 7(b). The noisy data is shown in Fig. 7(c).

APPENDIX B: RANDOM FOREST, DECISION TREE, SUPPORT VECTOR MACHINE, AND OTHERS

Algorithms including random forest, decision tree, support vector machine, as well as *k*NN can be easily implemented using the open-source ML libraries such as the scikit-learn library for Python. We also explore these options with our training data and conclude that, given the current training data, the predictability of these algorithms is not superior compared to *k*NN and FFNN. Instead, artifacts are more likely to appear. For example, the predicted results using the random forest and decision tree methods on both the noiseless training data and noisy training data are shown in Fig. 8. Compared to simple decision tree, random forest mitigates the errors due to bias and variance by considering a collection of decision trees. Therefore, the result is slightly more accurate and less noisy. The presence of noise in the training data does not significantly affect the results. However, due to the lack of data in the region where $\varepsilon_1 < -10$ and $\varepsilon_2 < 1$, both the random forest and decision tree predict the signal to be much larger than unity.

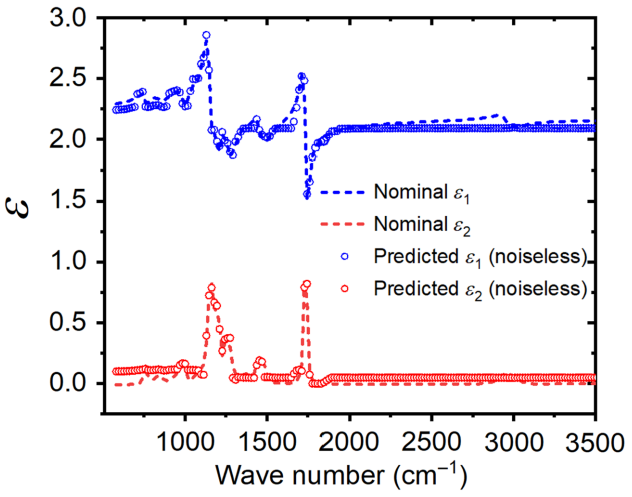

FIG. 9. Nominal dielectric function and predicted dielectric function using *k*NN on noiseless training data for PMMA.

We also explore other algorithms such as polynomial regression. However, no quantitatively accurate results are obtained even when a high polynomial order is used. This is due to the vast contrast between the fasting varying nature of S_2 as a function of ε near the origin and its slowly varying asymptotic behavior for large $|\varepsilon|$. Globally smooth functions such as polynomials are not suitable for approximating S_2.

APPENDIX C: THE INVERSE PROBLEM USING *K*NN

Similar to the FFNN case, algorithms such as *k*NN can be easily adapted to solve the reverse problem. However, the accuracy is found to be significantly worse compared to FFNN. For example, we test the inverse problem using *k*NN on the easiest target—PMMA, whose dielectric function is small. The procedure is similar to that of using FFNN and the result is shown in Fig. 9. Even with noiseless training data, the consistency is relatively poor with $>10\%$ error in some frequency ranges. Therefore, we conclude that given the current training data, *k*NN is not recommended for the reverse problem and FFNN remains the most accurate.

[1] X. Chen, D. Hu, R. Mescall, G. You, D. N. Basov, Q. Dai, and M. Liu, Modern scattering-type scanning near-field optical microscopy for advanced material research, Adv. Mater. **1804774**, 1804774 (2019).

[2] F. Keilmann and R. Hillenbrand, Near-field microscopy by elastic light scattering from a Tip, Philos. Trans. A. Math. Phys. Eng. Sci. **362**, 787 (2004).

[3] J. M. Atkin, S. Berweger, A. C. Jones, and M. B. Raschke, Nano-Optical imaging and spectroscopy of order, phases, and domains in complex solids, Adv. Phys. **61**, 745 (2012).

[4] R. Hillenbrand and F. Keilmann, Complex Optical Constants on a Subwavelength Scale, Phys. Rev. Lett. **85**, 3029 (2000).

[5] A. A. Govyadinov, S. Mastel, F. Golmar, A. Chuvilin, P. S. Carney, and R. Hillenbrand, Recovery of permittivity and depth from near-field data as a step toward infrared nanotomography, ACS Nano **8**, 6911 (2014).

[6] A. a. Govyadinov, I. Amenabar, F. Huth, P. S. Carney, and R. Hillenbrand, Quantitative measurement of local infrared absorption and dielectric function with Tip-enhanced near-field microscopy, J. Phys. Chem. Lett. **4**, 1526 (2013).

[7] S. G. Stanciu, D. E. Tranca, L. Pastorino, S. Boi, Y. M. Song, Y. J. Yoo, S. Ishii, R. Hristu, F. Yang, G. Bussetti, and G. A. Stanciu, Characterization of nanomaterials by locally determining their complex permittivity with scattering-type scanning near-field optical microscopy, ACS Appl. Nano Mater. **3**, 1250 (2020).

[8] D. E. Tranca, S. G. Stanciu, R. Hristu, C. Stoichita, S. a M. Tofail, and G. a Stanciu, High-Resolution quantitative determination of dielectric function by using scattering

scanning near-field optical microscopy, Sci. Rep. **5**, 11876 (2015).

[9] A. S. McLeod, E. van Heumen, J. G. Ramirez, S. Wang, T. Saerbeck, S. Guenon, M. Goldflam, L. Anderegg, P. Kelly, A. Mueller, M. K. Liu, I. K. Schuller, and D. N. Basov, Nanotextured phase coexistence in the correlated insulator V_2O_3, Nat. Phys. **13**, 80 (2016).

[10] G. X. Ni, A. S. McLeod, Z. Sun, L. Wang, L. Xiong, K. W. Post, S. S. Sunku, B.-Y. Jiang, J. Hone, C. R. Dean, M. M. Fogler, and D. N. Basov, Fundamental limits to graphene plasmonics, Nature **557**, 530 (2018).

[11] K. W. Post, A. S. McLeod, M. Hepting, M. Bluschke, Y. Wang, G. Cristiani, G. Logvenov, A. Charnukha, G. X. Ni, P. Radhakrishnan, M. Minola, A. Pasupathy, A. V. Boris, E. Benckiser, K. A. Dahmen, E. W. Carlson, B. Keimer, and D. N. Basov, Coexisting first- and second-order electronic phase transitions in a correlated oxide, Nat. Phys. **14**, 1056 (2018).

[12] X. Chen, X. Fan, L. Li, N. Zhang, Z. Niu, T. Guo, S. Xu, H. Xu, D. Wang, H. Zhang, A. S. McLeod, Z. Luo, Q. Lu, A. J. Millis, D. N. Basov, M. Liu, and C. Zeng, Moiré engineering of electronic phenomena in correlated oxides, Nat. Phys. **16**, 631 (2020).

[13] M. M. Qazilbash, M. Brehm, B.-G. Chae, P.-C. Ho, G. O. Andreev, B.-J. Kim, S. J. Yun, A. V. Balatsky, M. B. Maple, F. Keilmann, H.-T. Kim, and D. N. Basov, Mott transition in VO2 revealed by infrared spectroscopy and nano-imaging, Science **318**, 1750 (2007).

[14] Z. Fei, A. S. Rodin, G. O. Andreev, W. Bao, A. S. McLeod, M. Wagner, L. M. Zhang, Z. Zhao, M. Thiemens, G. Dominguez, M. M. Fogler, A. H. C. Neto, C. N. Lau, F. Keilmann, and D. N. Basov, Gate-Tuning of graphene plasmons revealed by infrared nano-imaging, Nature **487**, 82 (2012).

[15] S. Dai, Z. Fei, Q. Ma, A. S. Rodin, M. Wagner, A. S. McLeod, M. K. Liu, W. Gannett, W. Regan, K. Watanabe, T. Taniguchi, M. Thiemens, G. Dominguez, A. H. C. Neto, A. Zettl, F. Keilmann, P. Jarillo-Herrero, M. M. Fogler, and D. N. Basov, Tunable phonon polaritons in atomically thin van Der waals crystals of boron nitride, Science **343**, 1125 (2014).

[16] H.-G. von Ribbeck, M. Brehm, D. W. van der Weide, S. Winnerl, O. Drachenko, M. Helm, and F. Keilmann, Spectroscopic THz near-field microscope, Opt. Express **16**, 3430 (2008).

[17] H. A. Bechtel, E. A. Muller, R. L. Olmon, M. C. Martin, and M. B. Raschke, Ultrabroadband infrared nanospectroscopic imaging, Proc. Natl. Acad. Sci. **111**, 7191 (2014).

[18] J. Zhang, et al., Nano-Resolved Current-Induced Insulator-Metal Transition in the Mott Insulator Ca_2RuO_4, Phys. Rev. X **9**, 011032 (2019).

[19] O. Khatib, H. A. Bechtel, M. C. Martin, M. B. Raschke, and G. L. Carr, Far infrared synchrotron near-field nanoimaging and nanospectroscopy, ACS Photonics **5**, 2773 (2018).

[20] L. Wehmeier, D. Lang, Y. Liu, X. Zhang, S. Winnerl, L. M. Eng, and S. C. Kehr, Polarization-Dependent near-field phonon nanoscopy of oxides: $SrTiO_3$, *LiNb*O3, and $PbZr_{0.2}Ti_{0.8}O_3$, Phys. Rev. B **100**, 035444 (2019).

[21] B. Knoll and F. Keilmann, Enhanced dielectric contrast in scattering-type scanning near-field optical microscopy, Opt. Commun. **182**, 321 (2000).

[22] A. Cvitkovic, N. Ocelic, and R. Hillenbrand, Analytical model for quantitative prediction of material contrasts in scattering-type near-field optical microscopy, Opt. Express **15**, 8550 (2007).

[23] A. S. McLeod, P. Kelly, M. D. Goldflam, Z. Gainsforth, A. J. Westphal, G. Dominguez, M. H. Thiemens, M. M. Fogler, and D. N. Basov, Model for quantitative Tip-enhanced spectroscopy and the extraction of nanoscale-resolved optical constants, Phys. Rev. B **90**, 085136 (2014).

[24] S. T. Chui, X. Chen, M. Liu, Z. Lin, and J. Zi, Scattering of electromagnetic waves from a cone with conformal mapping: Application to scanning near-field optical microscope, Phys. Rev. B **97**, 081406 (2018).

[25] B.-Y. Jiang, L. M. Zhang, A. H. Castro Neto, D. N. Basov, and M. M. Fogler, Generalized spectral method for near-field optical microscopy, J. Appl. Phys. **119**, 054305 (2016).

[26] X. Chen, C. F. B. Lo, W. Zheng, H. Hu, Q. Dai, and M. Liu, Rigorous numerical modeling of scattering-type scanning near-field optical microscopy and spectroscopy, Appl. Phys. Lett. **111**, 223110 (2017).

[27] Y. Luan, L. McDermott, F. Hu, and Z. Fei, Tip- and Plasmon-Enhanced Infrared Nanoscopy for Ultrasensitive Molecular Characterizations, Phys. Rev. Appl. **13**, 034020 (2020).

[28] P. McArdle, D. J. Lahneman, A. Biswas, F. Keilmann, and M. M. Qazilbash, Near-field infrared nanospectroscopy of surface phonon-polariton resonances, Phys. Rev. Res. **2**, 023272 (2020).

[29] F. Mooshammer, M. A. Huber, F. Sandner, M. Plankl, M. Zizlsperger, and R. Huber, Quantifying nanoscale electromagnetic fields in near-field microscopy by Fourier demodulation analysis, ACS Photonics **7**, 344 (2020).

[30] S. Mastel, A. A. Govyadinov, C. Maissen, A. Chuvilin, A. Berger, and R. Hillenbrand, Understanding the image contrast of material boundaries in IR nanoscopy reaching 5 Nm spatial resolution, ACS Photonics **5**, 3372 (2018).

[31] G. Carleo, I. Cirac, K. Cranmer, L. Daudet, M. Schuld, N. Tishby, L. Vogt-Maranto, and L. Zdeborová, Machine learning and the physical sciences, Rev. Mod. Phys. **91**, 045002 (2019).

[32] Y. Zhang, A. Mesaros, K. Fujita, S. D. Edkins, M. H. Hamidian, K. Ch'ng, H. Eisaki, S. Uchida, J. C. S. Davis, E. Khatami, and E. A. Kim, Machine learning in electronic-quantum-matter imaging experiments, Nature **570**, 484 (2019).

[33] A. Krull, P. Hirsch, C. Rother, A. Schiffrin, and C. Krull, Artificial-Intelligence-Driven scanning probe microscopy, Commun. Phys. **3**, 54 (2020).

[34] T. Zhang, Q. Liu, Y. Dan, S. Yu, X. Han, J. Dai, and K. Xu, Machine learning and evolutionary algorithm studies of graphene metamaterials for optimized plasmon-induced transparency, Opt. Express **28**, 18899 (2020).

[35] S. An, C. Fowler, B. Zheng, M. Y. Shalaginov, H. Tang, H. Li, L. Zhou, J. Ding, A. M. Agarwal, C. Rivero-Baleine, K. A. Richardson, T. Gu, J. Hu, and H. Zhang, A deep learning approach for objective-driven All-dielectric metasurface design, ACS Photonics **6**, 3196 (2019).

[36] I. Tanriover, W. Hadibrata, and K. Aydin, A physics based approach for neural networks enabled design of All-dielectric metasurfaces, ACS Photonics **7**, 1957 (2020).

[37] J. Peurifoy, Y. Shen, L. Jing, Y. Yang, F. Cano-Renteria, B. G. DeLacy, J. D. Joannopoulos, M. Tegmark, and M. Soljačić, Nanophotonic particle simulation and inverse design using artificial neural networks, Sci. Adv. **4**, 4206 (2018).

[38] M. Autore, L. Mester, M. Goikoetxea, and R. Hillenbrand, Substrate matters: Surface-polariton enhanced infrared nanospectroscopy of molecular vibrations, Nano Lett. **19**, 8066 (2019).

[39] J. M. Stiegler, A. J. Huber, S. L. Diedenhofen, J. Gómez Rivas, R. E. Algra, E. P. A. M. Bakkers, and R. Hillenbrand, Nanoscale free-carrier profiling of individual semiconductor nanowires by infrared near-field nanoscopy, Nano Lett. **10**, 1387 (2010).

[40] F. Huth, M. Schnell, J. Wittborn, N. Ocelic, and R. Hillenbrand, Infrared-Spectroscopic nanoimaging with a thermal source, Nat. Mater. **10**, 352 (2011).

[41] X. Chen, J. Zhang, Z. Yao, H. A. Bechtel, M. C. Martin, G. L. Carr, and M. Liu, Ultrabroadband infrared near-field spectroscopy and imaging of local resonators in percolative gold films, J. Opt. Soc. Am. B **36**, 3315 (2019).

[42] B. Hauer, A. P. Engelhardt, and T. Taubner, Quasi-Analytical model for scattering infrared near-field microscopy on layered systems, Opt. Express **20**, 13173 (2012).

[43] E. D. Palik, *Handbook of Optical Constants of Solids* (Academic, San Diego, 1985).

[44] L. Jung, J. Pries, T. W. W. Maß, M. Lewin, D. S. Boyuk, A. T. Mohabir, M. A. Filler, M. Wuttig, and T. Taubner, Quantification of carrier density gradients along axially doped silicon nanowires using infrared nanoscopy, ACS Photonics **6**, 1744 (2019).

[45] C. Liewald, S. Mastel, J. Hesler, A. J. Huber, R. Hillenbrand, and F. Keilmann, All-Electronic terahertz nanoscopy, Optica **5**, 159 (2018).

[46] N. A. Aghamiri, F. Huth, A. J. Huber, A. Fali, R. Hillenbrand, and Y. Abate, Hyperspectral time-domain terahertz nano-imaging, Opt. Express **27**, 24231 (2019).

[47] V. V. Kozoderov and E. V. Dmitriev, Testing different classification methods in airborne hyperspectral imagery processing, Opt. Express **24**, A956 (2016).

[48] J. Kyoung, H. E. Kang, and S. W. Hwang, Surface plasmonometry: High-resolution and model-free plasmonic measurements of the refractive index and Its biosensing application, ACS Photonics **4**, 783 (2017).

[49] D. Ravi, C. Wong, F. Deligianni, M. Berthelot, J. Andreu-Perez, B. Lo, and G. Z. Yang, Deep learning for health informatics, IEEE J. Biomed. Heal. Informatics **1**, 4 (2017).

[50] A. Fadlalla and C. H. Lin, An analysis of the applications of neural networks in finance, Interfaces **4**, 112 (2001).

[51] H. K. D. H. Bhadeshia, Neural networks in materials science, ISIJ Int. **10**, 966 (1999).

[52] C. T. Kelley, Iterative Methods for Optimization (1999).

[53] F. Mooshammer, F. Sandner, M. A. Huber, M. Zizlsperger, H. Weigand, M. Plankl, C. Weyrich, M. Lanius, J. Kampmeier, G. Mussler, D. Grützmacher, J. L. Boland, T. L. Cocker, and R. Huber, Nanoscale near-field tomography of surface states on $(Bi_{0.5}Sb_{0.5})_2Te_3$, Nano Lett. **18**, 7515 (2018).

[54] D. E. Tranca, S. G. Stanciu, R. Hristu, B. M. Witgen, and G. A. Stanciu, Nanoscale mapping of refractive index by using scattering-type scanning near-field optical microscopy, nanomedicine nanotechnology, Biol. Med. **14**, 47 (2018).

[55] S. Tsuda, S. Yamaguchi, Y. Kanamori, and H. Yugami, Spectral and angular shaping of infrared radiation in a polymer resonator with molecular vibrational modes, Opt. Express **6**, 6899 (2018).

[56] S. C. Schneider, S. Grafström, and L. M. Eng, Scattering near-field optical microscopy of optically anisotropic systems, Phys. Rev. B **71**, 115418 (2005).

[57] K. Wang, D. M. Mittleman, N. C. J. Van Der Valk, and P. C. M. Planken, Antenna effects in terahertz apertureless near-field optical microscopy, Appl. Phys. Lett. **85**, 2715 (2004).

[58] X. Chen, X. Liu, X. Guo, S. Chen, H. Hu, E. Nikulina, X. Ye, Z. Yao, H. A. Bechtel, M. C. Martin, G. L. Carr, Q. Dai, S. Zhuang, Q. Hu, Y. Zhu, R. Hillenbrand, M. Liu, and G. You, THz near-field imaging of extreme subwavelength metal structures, ACS Photonics **7**, 687 (2020).

[59] A. Pizzuto, D. M. Mittleman, and P. Klarskov, Laser THz emission nanoscopy and THz nanoscopy, Opt. Express **28**, 18778 (2020).

[60] M. Liu, A. J. Sternbach, and D. N. Basov, Nanoscale electrodynamics of strongly correlated quantum materials, Rep. Prog. Phys. **80**, 014501 (2017).

[61] B. T. O'Callahan, A. C. Jones, J. Hyung Park, D. H. Cobden, J. M. Atkin, and M. B. Raschke, Inhomogeneity of the ultrafast insulator-to-metal transition dynamics of VO_2, Nat. Commun. **6**, 6849 (2015).

[62] J. Chen, M. Badioli, P. Alonso-González, S. Thongrattanasiri, F. Huth, J. Osmond, M. Spasenović, A. Centeno, A. Pesquera, P. Godignon, A. Zurutuza Elorza, N. Camara, F. J. G. de Abajo, R. Hillenbrand, and F. H. L. Koppens, Optical nano-imaging of gate-tunable graphene plasmons, Nature **487**, 77 (2012).

[63] X. G. Xu, J. H. Jiang, L. Gilburd, R. G. Rensing, K. S. Burch, C. Zhi, Y. Bando, D. Golberg, and G. C. Walker, Mid-Infrared polaritonic coupling between boron nitride nanotubes and graphene, ACS Nano **8**, 11305 (2014).

[64] M. Chen, X. Lin, T. H. Dinh, Z. Zheng, J. Shen, Q. Ma, H. Chen, P. Jarillo-Herrero, and S. Dai, Configurable phonon polaritons in twisted α-MoO_3, Nat. Mater. **19**, 1307 (2020).

[65] W. Ma, P. Alonso-González, S. Li, A. Y. Nikitin, J. Yuan, J. Martín-Sánchez, J. Taboada-Gutiérrez, I. Amenabar, P. Li, S. Vélez, C. Tollan, Z. Dai, Y. Zhang, S. Sriram, K. Kalantar-Zadeh, S.-T. Lee, R. Hillenbrand, and Q. Bao, In-Plane anisotropic and ultra-Low-loss polaritons in a natural van Der waals crystal, Nature **562**, 557 (2018).